

## PAPER



Cite this: *J. Mater. Chem. C*, 2019,  
7, 863

## Inorganic CsBi<sub>3</sub>I<sub>10</sub> perovskite/silicon heterojunctions for sensitive, self-driven and air-stable NIR photodetectors†

Xiao-Wei Tong,<sup>a</sup> Zhi-Xiang Zhang,<sup>a</sup> Di Wang,<sup>a</sup> Lin-Bao Luo,<sup>ib</sup>\*<sup>a</sup> Chao Xie\*<sup>a</sup> and Yu-Cheng Wu<sup>ib</sup>\*<sup>b</sup>

In this study, a sensitive near-infrared (NIR) photodetector based on a CsBi<sub>3</sub>I<sub>10</sub> perovskite/Si heterojunction is developed by directly coating a layer of inorganic perovskite onto a planar Si substrate. The as-constructed heterojunction displays a representative current rectifying behavior in the dark and remarkable photoresponse properties upon light irradiation. The distinct photovoltaic effect enables the device to function as a self-driven photodetector working at zero bias. Furthermore, it is observed that the photodetector is sensitive in a wide spectral region with peak sensitivity at ~820 nm. Under 808 nm illumination, the critical photoresponse parameters of responsivity, external quantum efficiency and specific detectivity reached 178.7 mA W<sup>-1</sup>, 27.2% and 4.99 × 10<sup>10</sup> Jones at zero bias, respectively, which can be further increased to as high as 492.1 mA W<sup>-1</sup>, 75.2% and 1.38 × 10<sup>11</sup> Jones at a working bias of -1 V. What is more, the present device also holds a large *I*<sub>light</sub>/*I*<sub>dark</sub> ratio of ~1 × 10<sup>4</sup>, a rapid response speed of 73/36 μs, and excellent air stability even after 3 months of storage under ambient conditions. Considering the good photoresponse performance and facile assembly approach, the CsBi<sub>3</sub>I<sub>10</sub> perovskite/Si heterojunction possesses huge potential for future cost-effective and high-performance photodetection applications.

Received 16th November 2018,  
Accepted 8th December 2018

DOI: 10.1039/c8tc05765f

rsc.li/materials-c

## Introduction

Metal halide perovskites have recently attracted extensive attention worldwide because of their diverse facile synthesis methods, low exciton binding energy, tunable direct band gap, long carrier diffusion length, high carrier mobility, and large optical absorption coefficient, *etc.*<sup>1</sup> These extraordinary material properties make perovskites a promising class of building blocks for a variety of new generation optoelectronic devices, such as solar cells,<sup>2–4</sup> light emitting diodes (LEDs),<sup>5–7</sup> solid-state lasers,<sup>8,9</sup> and photodetectors.<sup>10–13</sup> Among these devices, photodetectors, which can directly convert optical signals into electrical signals and are of critical importance for a wide range of military and civilian applications, have been extensively explored with

photoactive perovskite materials.<sup>14–17</sup> So far, significant progress has been achieved in perovskite-based photodetectors with high device performance. For example, Yang's group developed a high-performance solution-processed hybrid perovskite photodetector.<sup>12</sup> Taking advantage of a novel hole-blocking layer, the dark current density was greatly suppressed, and the device achieved a large specific detectivity approaching 10<sup>14</sup> Jones. By designing hybrid perovskite phototransistors exploiting the pronounced photo-gating effect, ultrahigh responsivities exceeding 10<sup>9</sup> A W<sup>-1</sup> in a broad spectral region have also been realized recently.<sup>18,19</sup> In spite of the gratifying success, there still exist some obstacles that hinder the large-scale application of photodetectors made from extensively used organic–inorganic hybrid perovskites. For instance, the most severe ones are the toxicity of environmentally unfriendly Pb atoms, as well as the poor air stability because of the involvement of organic components.<sup>20–22</sup> Up to now, several approaches have been developed to address these problems, such as substituting Pb atoms with other nontoxic atoms<sup>23</sup> and exploring some new perovskite materials.<sup>24</sup> Recently, our group has also observed that the nontoxic, inorganic CsBi<sub>3</sub>I<sub>10</sub> perovskite holds outstanding optical and optoelectrical features and is highly sensitive to red light illumination.<sup>25</sup> What is more, the excellent photoresponse characteristics along with the good air stability make this perovskite material extremely suitable for high-performance photodetection applications.

<sup>a</sup> School of Electronic Sciences and Applied Physics, Hefei University of Technology, Hefei, Anhui 230009, China. E-mail: luolb@hfut.edu.cn, chao.xie@hfut.edu.cn

<sup>b</sup> School of Materials Science and Engineering and Anhui Provincial Key Laboratory of Advanced Functional Materials and Devices, Hefei University of Technology, Hefei, Anhui 230009, China. E-mail: ycwu@hfut.edu.cn

† Electronic supplementary information (ESI) available: Schematic illustration of the fabrication procedure of the CsBi<sub>3</sub>I<sub>10</sub>/Si heterojunction photodetector. The dependence of  $(xh\nu)^2$  on  $h\nu$  for the CsBi<sub>3</sub>I<sub>10</sub> perovskite. UPS spectrum of the CsBi<sub>3</sub>I<sub>10</sub> perovskite film. *I*-*V* characteristics of the CsBi<sub>3</sub>I<sub>10</sub> perovskite/Si heterojunction photodetector in the dark and under 808 nm light illumination with varied light intensities. See DOI: 10.1039/c8tc05765f

High-frequency optical sensing is essential for many crucial applications including high-speed optical communication, fast data transmission, military warning and rapid imaging, *etc.*<sup>26</sup> Therefore, it is necessary to develop highly sensitive photodetectors with fast response speed to meet the requirements of practical applications. Many recent studies have shown that perovskite photodiodes, which are characterized by the inherent built-in electric field that facilitates rapid separation and transport of photocarriers, usually exhibit faster response speeds with a lower noise than other types of perovskite photodetectors.<sup>27,28</sup> Hitherto, an intrinsic response rate in the level of nanoseconds has been achieved in perovskite photodiodes.<sup>29</sup> However, these photodetectors with solar cell-like geometries typically have complicated device architectures and require complex multiple patterning steps for construction.<sup>14,15</sup> In addition, the involvement of organic semiconductors serving as electron/hole transporting layers for photocarrier extraction also inevitably degrades air stability and long-term durability of the detectors. Such a circumstance greatly limits the wide application of perovskite photodiodes. A promising avenue is to integrate perovskite materials with traditional inorganic optoelectronic semiconductors having mature processing technologies to form heterojunction photodetectors. Prospectively, the combination will not only simplify device geometry and minimize processing cost, but also exploit the complementary properties of both materials, which is beneficial for device performance enhancement and may bring about some new functionalities.<sup>30,31</sup>

In this work, we present a sensitive NIR photodetector by directly depositing a layer of CsBi<sub>3</sub>I<sub>10</sub> perovskite onto a planar Si substrate. It is observed that the as-assembled heterojunction displays a pronounced rectifying behavior with a rectification ratio of  $\sim 4 \times 10^2$  at a working bias of  $\pm 1$  V in the dark. Upon 808 nm NIR illumination, the device exhibits an evident photovoltaic effect, endowing the detector with the capability of sensing light illumination without an exterior power supply. Further optoelectronic study finds that the heterojunction photodetector is sensitive in a broad spectral region with the peak sensitivity at the light wavelength of  $\sim 820$  nm. At zero bias, the  $I_{\text{light}}/I_{\text{dark}}$  ratio, responsivity, external quantum efficiency (EQE) and specific detectivity are  $\sim 1 \times 10^4$ , 178.7 mA W<sup>-1</sup>, 27.2% and  $4.99 \times 10^{10}$  Jones, respectively. The responsivity, EQE and specific detectivity can be further improved to 492.1 mA W<sup>-1</sup>, 75.2% and  $1.38 \times 10^{11}$  Jones, respectively, by applying an operational bias of  $-1$  V. What is more, the photodetector exhibits a rapid response rate with rise/decay times of 73/36  $\mu$ s. Such a good device performance is believed to be directly related to the high-quality heterojunction formed at the CsBi<sub>3</sub>I<sub>10</sub>/Si interface. In addition, the photoresponse properties can remain almost unaffected after 3 months of storage under ambient conditions, validating robust long-term durability and superior air stability. The generality of the above results together with the solution processability implies that the present heterojunction photodetector is highly promising for future high-performance, cost-effective NIR photodetection applications.

## Results and discussion

Fig. 1(a) and (b) depict a schematic diagram and photograph of the CsBi<sub>3</sub>I<sub>10</sub> perovskite/Si heterojunction NIR photodetector, which was obtained by directly spin-coating a layer of CsBi<sub>3</sub>I<sub>10</sub> perovskite onto a planar Si substrate. The detailed device fabrication procedure is provided in the Experimental section and shown in Fig. S1 (ESI<sup>†</sup>). Fig. 1(c) shows the cross-sectional scanning electron microscopy (SEM) image of a typical CsBi<sub>3</sub>I<sub>10</sub>/Si heterojunction, from which both the perovskite film and Si substrate can be easily distinguished. It is observed that the perovskite film with a thickness of  $\sim 1$   $\mu$ m forms intimate contact with the Si substrate. Fig. S2 (ESI<sup>†</sup>) displays a typical top-view SEM image of the CsBi<sub>3</sub>I<sub>10</sub> film. It can be seen that the sample has a uniform surface with many holes which were attributed to the relatively fast solvent evaporation process. X-ray diffraction (XRD) characterization was conducted to study the phase of the as-prepared CsBi<sub>3</sub>I<sub>10</sub> perovskite on the Si substrate. As depicted in Fig. 1(d), the XRD pattern is characterized by a series of representative diffraction peaks located at 12.8°, 25.8°, and 41.6°, which can be readily indexed to the (003), (006), and (300) planes of the rhombohedra phase of BiI<sub>3</sub>, respectively. The result is in accordance with our previous observation of the CsBi<sub>3</sub>I<sub>10</sub> perovskite prepared on a glass substrate,<sup>25</sup> suggesting that the CsBi<sub>3</sub>I<sub>10</sub> perovskite here also possesses a layered crystal structure containing partially broken zero-dimensional structures like Cs<sub>3</sub>Bi<sub>2</sub>I<sub>9</sub> between the layers.<sup>32</sup> Furthermore, X-ray photoelectron spectroscopy (XPS) analysis was carried out to determine the components and binding energies of the CsBi<sub>3</sub>I<sub>10</sub> perovskite, as shown in Fig. 1e and f. The peaks at 738.93, 724.93, 619.38, 630.78, 158.98 and 164.23 eV are related to Cs 3d<sub>3/2</sub>, Cs 3d<sub>5/2</sub>, I 3d<sub>5/2</sub>, I 3d<sub>3/2</sub>, Bi 4f<sub>7/2</sub> and Bi 4f<sub>5/2</sub> orbitals, respectively. The above results confirm the existence of Cs, Bi and I elements in the as-synthesized sample.

We first studied the electrical characteristics of a representative CsBi<sub>3</sub>I<sub>10</sub>/Si heterojunction in the dark. Fig. 2(a) depicts the current–voltage (*I*–*V*) curve of the device on both linear and logarithmic scales. The heterojunction displayed a typical current rectifying behavior, and the rectification ratio was estimated to be  $\sim 4 \times 10^2$  within  $\pm 1$  V. In light of the good ohmic contact of both CsBi<sub>3</sub>I<sub>10</sub> perovskite/Au and n-Si/In–Ga

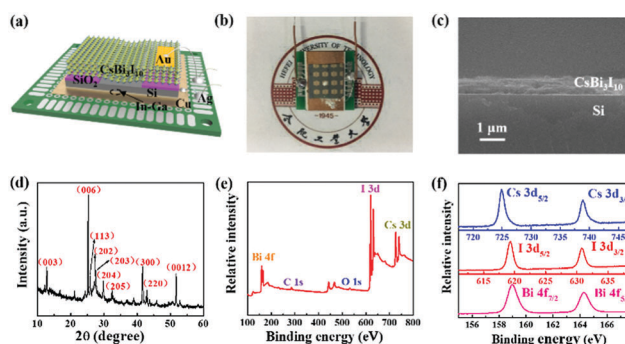


Fig. 1 (a) Schematic diagram and (b) photograph of the CsBi<sub>3</sub>I<sub>10</sub> perovskite/Si heterojunction photodetector. (c) Cross-sectional SEM image of the CsBi<sub>3</sub>I<sub>10</sub> perovskite/Si heterojunction. (d) XRD pattern of the CsBi<sub>3</sub>I<sub>10</sub> perovskite film. (e and f) XPS spectra of the CsBi<sub>3</sub>I<sub>10</sub> perovskite film.

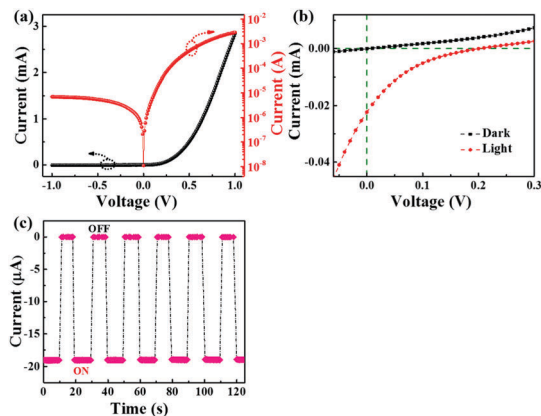


Fig. 2 (a)  $I$ - $V$  characteristics of the  $\text{CsBi}_3\text{I}_{10}$  perovskite/Si heterojunction in the dark. (b)  $I$ - $V$  curves of the heterojunction photodetector in darkness and under 808 nm light illumination. (c) Time-dependent photoresponse of the photodetector under 808 nm light illumination at zero bias.

structures,<sup>25,33</sup> the above nonlinear  $I$ - $V$  behavior should originate exclusively from the heterojunction formed between the perovskite and Si. Next, the photoresponse properties of the  $\text{CsBi}_3\text{I}_{10}$  perovskite/Si heterojunction were probed. Fig. 2(b) shows the  $I$ - $V$  characteristics of the device in the dark and under 808 nm NIR illumination with a light intensity of  $50.3 \text{ mW cm}^{-2}$ , respectively. Significantly, the heterojunction demonstrated an obvious photovoltaic effect with an open-circuit voltage ( $V_{\text{OC}}$ ) and a short-circuit current ( $I_{\text{SC}}$ ) of  $\sim 0.205 \text{ V}$  and  $\sim 22.27 \text{ } \mu\text{A}$ , respectively. Although the energy conversion efficiency was less than 1%, such an effect can endow our detector with the capability of operating as a self-driven photodiode working at zero bias. The time-dependent photoresponse of the heterojunction upon alternately switched 808 nm irradiation was further recorded at zero bias. As observed in Fig. 2(c), the detector can be readily switched between high- and low-conductance states, reaching a large  $I_{\text{light}}/I_{\text{dark}}$  ratio as high as  $\sim 1 \times 10^4$  with good reversibility. What is more, the photoresponse curve presented steep rise and fall edges, which not only suggests a rapid response rate, but also implies a fast separation and collection process of photocarriers in the heterojunction.

The photoresponse properties of the perovskite/Si heterojunction photodetector depended strongly on the incident light wavelength. Fig. 3(a) summarizes the  $I$ - $V$  curves of the device under irradiations with different wavelengths of 254, 365, 650, 808, and 980 nm at a constant intensity ( $ca. 1 \text{ mW cm}^{-2}$ ). Obviously, relatively strong photovoltaic behaviors were observed for visible and NIR irradiations, and the strongest was found at the wavelength of 808 nm, while the photodetector exhibited very weak photovoltaic activities under UV illuminations. The time-dependent response curves under zero bias at these wavelengths were also recorded and are shown in Fig. 3(b) and (c). It was found that the photocurrent was only  $\sim 75 \text{ nA}$  at wavelengths of 254 and 365 nm, while it increased drastically to  $\sim 1.0 \text{ } \mu\text{A}$  at wavelengths of 650 and 980 nm, and further to the maximum value of  $\sim 1.75 \text{ } \mu\text{A}$  at the wavelength of 808 nm. Such a variation trend is in good agreement with that of the short-circuit current

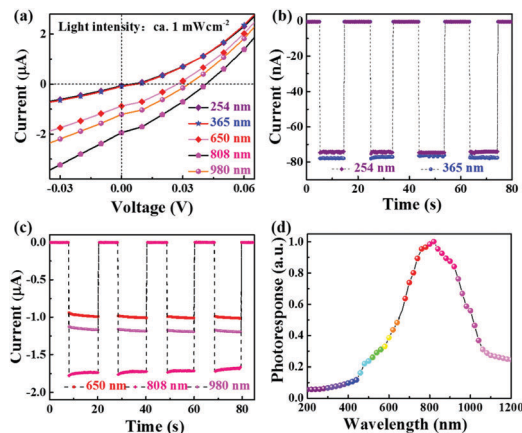


Fig. 3 (a)  $I$ - $V$  curves of the  $\text{CsBi}_3\text{I}_{10}$  perovskite/Si heterojunction photodetector under 254, 365, 650, 808 and 980 nm light illumination with a constant intensity of  $ca. 1 \text{ mW cm}^{-2}$ . (b) and (c) Time-dependent photoresponse of the photodetector under light illumination with different wavelengths at zero bias. (d) Spectral photoresponse of the heterojunction photodetector at zero bias.

in the  $I$ - $V$  curves depicted in Fig. 3(a). To shed light on the relationship between photoresponse and incident light wavelength, the spectral response of the perovskite/Si heterojunction device was further studied at zero bias. As illustrated in Fig. 3(d), the photoresponse first rose slowly and then steeply when increasing the light wavelength from 200 to 500 nm and then from 500 to 820 nm, respectively. Further increasing the light wavelength led to a decrease in the photoresponse. Such a spectral selectivity is in good accordance with the EQE as a function of wavelength (Fig. S3, ESI<sup>†</sup>). It is noteworthy that the spectral response of the current heterojunction photodetector was in stark contrast to that of a traditional Si photodiode and a  $\text{CsBi}_3\text{I}_{10}$  perovskite-based photoconductive detector in our previous work.<sup>25</sup>

The above abnormal spectral response can be understood by correlating the response characteristics with the optical property and energy band diagram of the  $\text{CsBi}_3\text{I}_{10}$  perovskite/Si heterojunction. Fig. 4(a) depicts the optical absorption spectrum of the  $\text{CsBi}_3\text{I}_{10}$  perovskite/Si hybrid, along with that of the pure  $\text{CsBi}_3\text{I}_{10}$  perovskite and bare planar Si substrate for comparison. Apparently, the perovskite/Si hybrid showed wide optical absorption in the wavelength region of 400–1200 nm. Compared with the pure perovskite, the perovskite/Si hybrid displayed only slight improvement at wavelengths shorter than  $\sim 700 \text{ nm}$ , while showing significant enhancement at wavelengths longer than  $\sim 700 \text{ nm}$  in its optical absorption curve. Furthermore, by extrapolating the curve of  $(\alpha h\nu)^2 - h\nu$  derived from the absorption spectrum, where  $\alpha$  is absorbance,  $h$  is Planck's constant, and  $\nu$  is frequency, the band gap of the perovskite was estimated to be  $\sim 1.77 \text{ eV}$  (the value corresponds to the band edge absorption cutoff wavelength of  $\sim 700 \text{ nm}$ ; Fig. S4(a), ESI<sup>†</sup>). The above results suggested that optical absorption mainly took place within the perovskite layer at light wavelengths below  $\sim 700 \text{ nm}$ , while it occurred primarily within the underlying Si substrate at light wavelengths exceeding  $\sim 700 \text{ nm}$  in the present perovskite/Si heterojunction. In addition,

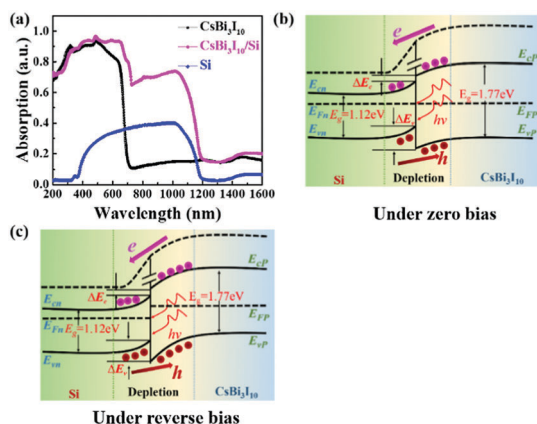


Fig. 4 (a) Absorption spectra of the CsBi<sub>3</sub>I<sub>10</sub> perovskite/Si hybrid, pure CsBi<sub>3</sub>I<sub>10</sub> perovskite film and bare planar Si. Energy band diagrams of the CsBi<sub>3</sub>I<sub>10</sub> perovskite/Si heterojunction under light illumination at (b) zero bias and (c) reverse bias.

according to the ultraviolet photoemission spectroscopy (UPS) study shown in Fig. S4(b) (ESI<sup>†</sup>), the CsBi<sub>3</sub>I<sub>10</sub> perovskite used here is a weakly p-type semiconductor, and its Fermi level, conduction band minimum (CBM), and valence band maximum (VBM) were deduced to be  $\sim 5.82$ ,  $\sim 4.66$  and  $6.33$  eV, respectively. Roughly, the Fermi level of n-Si with a resistivity of 1–10  $\Omega$  cm was estimated to be  $\sim 4.25$  eV.<sup>34</sup> Therefore, when the perovskite contacted with n-Si, to attain thermal equilibrium, electrons diffused from Si to the perovskite until the Fermi levels aligned at the same level. In the meantime, such an electron diffusion process caused the energy levels near the Si (perovskite) surface to bend upward (downward), indicating the emergence of a built-in electric field within the depletion region at the perovskite/Si interface [Fig. 4(b)]. Upon illuminated by the irradiation, electron–hole pairs were generated primarily within either perovskite at light wavelengths shorter than  $\sim 700$  nm or Si at light wavelengths longer than  $\sim 700$  nm, due to the unique optical property of the heterojunction discussed previously. The electrons and holes then diffused to the depletion region and were separated by the built-in electric field and ultimately collected by the respective electrodes, leading to the generation of photocurrent. However, defects and trap states that act as carrier recombination centers exist inevitably in spin-coated perovskite layers, due to the relatively poor quality of the polycrystalline film.<sup>35</sup> Therefore, part of the photocarriers generated in the perovskite layer cannot arrive at the depletion region and contribute to the photocurrent before recombination, which explains the relatively low photoresponse at the light wavelength region below  $\sim 700$  nm. In particular, because of the large optical absorption coefficient of the CsBi<sub>3</sub>I<sub>10</sub> perovskite in the UV wavelength region,<sup>32</sup> the incident UV light tends to be absorbed near the surface of the film. Thus, photocarriers induced by UV irradiation require a longer distance to diffuse to the depletion region, leading to a more severe recombination and therefore poorer photoresponse. Another reason could be associated with the tradeoff between the number and energy of the incident photons. Because of higher photon energy, UV irradiation with identical light intensity can excite less electron–hole pairs with contribution to

photocurrent, in comparison with visible and NIR illumination. It should be pointed out that although the heterojunction photodetector exhibited poor photoresponse at the short wavelength region, the unique optical property provided the present device with excellent spectral selectivity.

We further investigated the dependence of the photoresponse properties on incident light intensity. Fig. 5(a) shows the  $I$ - $V$  curves of the heterojunction photodetector upon 808 nm irradiation with varied light intensities from 0.11 to 50.3  $\text{mW cm}^{-2}$ , and the corresponding enlarged  $I$ - $V$  curves are illustrated in Fig. S5 (ESI<sup>†</sup>). Remarkably, the photocurrent at both zero and reverse biases rose monotonously with increasing light intensity, which is understandable since incident light with a higher intensity can induce more photocarriers. Time-dependent photoresponse curves at different light intensities were also recorded. As plotted in Fig. 5(b), the dark current can remain almost invariant for all illuminating conditions, while the photocurrent increased gradually with increasing light intensity. What is more, the device can also be readily switched between high- and low-conductance states, suggesting that the present photodetector can operate properly upon illumination with a wide light intensity range. To deeply understand such a relationship, the net photocurrent was extracted by deducing the current under illumination with dark current, and plotted as a function of incident light intensity as illustrated in Fig. 5(c).

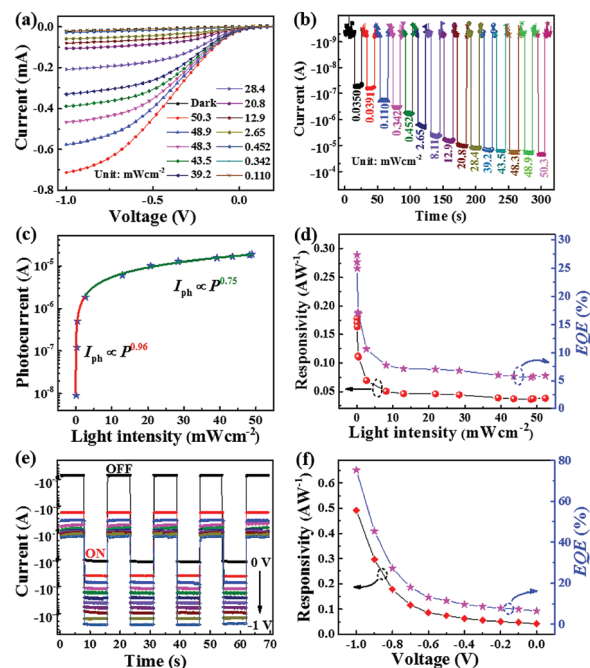


Fig. 5 (a)  $I$ - $V$  characteristics of the CsBi<sub>3</sub>I<sub>10</sub> perovskite/Si heterojunction photodetector in darkness and under 808 nm light illumination with varied light intensities. (b) Time-dependent photoresponse of the photodetector under 808 nm light irradiation at different intensities. (c) Photocurrent of the photodetector as a function of incident light intensity at zero bias. (d) Both responsivity and EQE of the device as a function of incident light intensity at zero bias. (e) Time-dependent photoresponse of the photodetector at zero and different reverse bias voltages. (f) Both responsivity and EQE of the device as a function of reverse bias voltage.

It was observed that with light intensity changed from 0.11 to 2.65 mW cm<sup>-2</sup>, the photocurrent increased swiftly from 8.98 nA to 1.84 μA, and a further increase in light intensity resulted in a slow rise in photocurrent. The cause of this phenomenon can be understood by fitting the relationship of the photocurrent with light intensity to a widely used power law:  $I_{\text{ph}} = AP^\theta$ ,<sup>36,37</sup> where  $I_{\text{ph}}$  is the photocurrent,  $A$  is a constant for 808 nm,  $P$  is the light intensity, and  $\theta$  is an empirical value relating to the photocarrier recombination activity. Interestingly, we found that fitting the curve in different light intensity ranges gave completely varied results: In a low light intensity region, close to an ideal value of  $\theta = 0.96$  was obtained, while a non-ideal exponent  $\theta = 0.75$  was achieved in a high light intensity regime. Such findings implied that recombination loss was very weak at low light intensity and became violent at high light intensity.<sup>38</sup> Therefore, the slow increase in photocurrent at the high light intensity region could be ascribed to the intensified photocarrier recombination, which was probably due to the high concentration of photoinduced carriers and the presence of trap states between the Fermi level and conduction band edge of the materials.<sup>39</sup>

To quantitatively assess the photoresponse performance of the present device, several important performance figures of merit including responsivity ( $R$ ), external quantum efficiency (EQE) and specific detectivity ( $D^*$ ), were then calculated.  $R$  is defined as the ratio between photocurrent and the total incident light power on the active area of a photodetector, while EQE is the ratio between the number of photoinduced electron-hole pairs with contribution to photocurrent and the total number of incident photons. On the other hand,  $D^*$  represents the capability of a photodetector to sense weak optical signals. These performance parameters are usually described by the following formulas:<sup>37,40,41</sup>

$$R = \frac{I_{\text{p}} - I_{\text{d}}}{P_{\lambda} S} \quad (1)$$

$$\text{EQE} = \frac{hcR_{\lambda}}{e\lambda} \quad (2)$$

$$D^* = \frac{R_{\lambda} A^{1/2}}{(2eI_{\text{d}})^{1/2}} \quad (3)$$

where  $I_{\text{p}}$ ,  $I_{\text{d}}$ ,  $P_{\lambda}$ ,  $S$ ,  $h$ ,  $c$ ,  $e$ ,  $\lambda$  and  $A$  denote photocurrent, dark current, incident light intensity, effective illuminating area ( $S = 0.01 \text{ cm}^2$ ), Planck's constant, velocity of light, elementary

charge, wavelength of the incident light, and effective area of the photodetector ( $A = 0.01 \text{ cm}^2$ ), respectively. Accordingly,  $R$ , EQE and  $D^*$  were estimated to be 178.7 mA W<sup>-1</sup>, 27.5% and  $4.99 \times 10^{10}$  Jones, respectively, at a low light intensity ( $35 \mu\text{W cm}^{-2}$ ) at zero bias. Fig. 5(d) plots  $R$  and EQE as a function of incident light intensity. Apparently, both values decreased with increasing light intensity, which further manifested the presence of nonnegligible recombination loss in the current photodetector at high light intensity.

Furthermore, we found that the photoresponse properties of the CsBi<sub>3</sub>I<sub>10</sub> perovskite/Si heterojunction photodetector also highly depended on the operational bias voltage. Fig. 5(e) shows the time-dependent photoresponse of the device at zero and different reverse biases upon periodically switched NIR illumination at a constant intensity of 2.65 mW cm<sup>-2</sup>. Obviously, the photocurrent increased monotonously with the increase of reverse bias, and the value was significantly enhanced by more than 2 orders of magnitude from  $\sim 1.15 \mu\text{A}$  to  $\sim 0.26 \text{ mA}$  when increasing the working voltage from 0 to  $-1 \text{ V}$ . However, further analysis found no obvious enhancement in the  $I_{\text{light}}/I_{\text{dark}}$  ratio, and the value even decreased slightly at some reverse working biases, due to the remarkably increased dark current at reverse bias, compared with the result at 0 V bias. Even so, the net photocurrent still rose with increasing reverse bias, which could be explained by the following two aspects. Under reverse bias, an exterior electric field with the same direction as the built-in one can significantly boost the separation and drift efficiency of photocarriers, and thus restrain their recombination activities.<sup>30</sup> In addition, applying a reverse bias can also extend the depletion region at the heterojunction interface, which affords more photocarriers to take part in the generation of photocurrent [Fig. 4(c)]. The  $R$  and EQE values of the device at different reverse biases were also calculated and are plotted in Fig. 5(f). Similar to the photocurrent, both  $R$  and EQE increased with the rise of reverse working bias, attaining maximum values of 492.1 mA W<sup>-1</sup> and 75.28% at the bias of  $-1 \text{ V}$ , respectively. Additionally, the  $D^*$  value was enhanced by nearly 3 times to  $1.38 \times 10^{11}$  Jones. Significantly, these performance parameters were comparable to or even better than those of previously reported perovskite-based photodiodes<sup>42-44</sup> and Si-based heterojunction photodetectors<sup>33,45,46</sup> with similar device geometries, as summarized in Table 1.

To evaluate the capability of our photodetector for detecting high-speed optical signals, we further characterized the response speed of the device by using an 808 nm laser diode powered by a function generator as the ultrafast light source. Fig. 6(a) plots the schematic setup for measuring response speed, and a digital

**Table 1** Comparison of photoresponse parameters of the device in this work with previously reported photodetectors with similar device geometries

Device structure	$R$ (A W <sup>-1</sup> )	$D^*$ (Jones)	$I_{\text{light}}/I_{\text{dark}}$ ratio	$\tau_{\text{r}}/\tau_{\text{f}}$ (ms)	Ref.
CsBi <sub>3</sub> I <sub>10</sub> /Si	0.492	$1.38 \times 10^{11}$	$\sim 10^4$	0.073/0.036	This work
MAPbI <sub>3</sub> /ZnO NRs <sup>a</sup>	0.0083	$\sim 1.5 \times 10^{10}$	$\sim 10^5$	0.053/0.063	42
MAPbI <sub>3</sub> /TiO <sub>2</sub> NRs	0.85	$7.8 \times 10^{10}$	150	—	43
MAPbI <sub>3</sub> /ZnO NRs	0.22	$9.3 \times 10^9$	—	300/800	44
CuO/SiNWs <sup>b</sup> array	$0.64 \times 10^{-4}$	$7.6 \times 10^8$	$\sim 10^4$	0.060/0.080	45
rGO <sup>c</sup> /Si	1.52	—	$> 10^4$	2/3.7	46
CQDs <sup>d</sup> /SiNWs array	0.353	—	$3 \times 10^3$	0.010/0.040	33

<sup>a</sup> Denotes nanorods. <sup>b</sup> Denotes Si nanowires. <sup>c</sup> Denotes reduced graphene oxide. <sup>d</sup> Denotes carbon quantum dots.

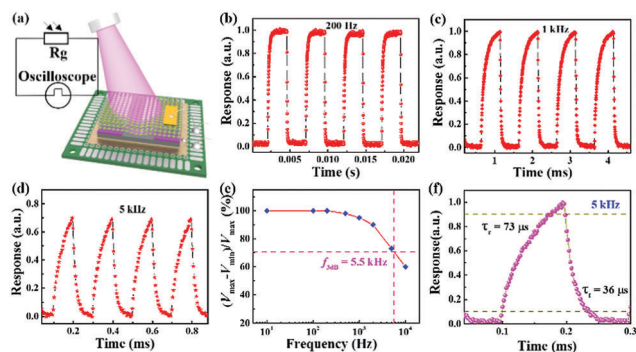


Fig. 6 (a) Schematic illustration of the setup for response speed measurement. (b) Photoresponse of the CsBi<sub>3</sub>I<sub>10</sub> perovskite/Si heterojunction photodetector under pulsed 808 nm light at the frequency of (b) 200 Hz, (c) 1 kHz, and (d) 5 kHz. (e) Relative balance  $(V_{\max} - V_{\min})/V_{\max}$  versus switching frequency of incident light. (f) A single enlarged cycle of photoresponse for estimating rise and fall times.

oscilloscope was employed to record the temporal photoresponse signal (photovoltage against time) in this study. Fig. 6(b)–(d) displays the photoresponse of the heterojunction photodetector to pulsed light of different modulating frequencies. Apparently, for all frequencies of 200, 1000 and 5000 Hz, the device demonstrated good switching characteristics with excellent repeatability, suggesting a rapid response speed of our photodetector. We further summarized the dependence of the relative balance  $(V_{\max} - V_{\min})/V_{\max}$  of the photoresponse on switching frequency, as shown in Fig. 6(e). It was found that the relative balance declined very slowly with the increase of modulating frequency, and it only decreased by  $\sim 40\%$  at a high frequency of 10 kHz. From the curve in Fig. 6(e), the 3 dB bandwidth, which describes the frequency for the photoresponse to decline to 70.7% of its maximum value, was estimated to be  $\sim 5.5$  kHz. In addition, we calculated the response time of the device as well. The rise/fall times were typically defined as the duration needed for the photoresponse to rise/decline from 10%/90% to 90%/10% of its peak value, respectively.<sup>33</sup> According to a magnified photoresponse curve at 5 kHz [Fig. 6(f)], the rise and fall times were deduced to be 73 and 36  $\mu\text{s}$ , respectively, which were comparable to those of the MAPbI<sub>3</sub> perovskite/ZnO nanorod heterojunction (53/63  $\mu\text{s}$ )<sup>42</sup> and the CuO/Si nanowire array heterojunction (60/80  $\mu\text{s}$ ) photodetectors in previous work.<sup>45</sup> The above results signified that the present CsBi<sub>3</sub>I<sub>10</sub> perovskite/Si heterojunction photodetector was able to sense fast varied optical signals, and therefore held great potential for future high-frequency optical sensing applications.

Another obvious advantage of the present CsBi<sub>3</sub>I<sub>10</sub> perovskite/Si heterojunction photodetector lies in its good durability and long-term stability under ambient conditions, both of which are critical for its real-life applications. Fig. 7(a) depicts the time-dependent photoresponse under continuously switched NIR light illumination. Apparently, the detector can work properly after 800 cycles of operation with almost identical dark current and photocurrent for each cycle, suggesting excellent durability of the photodetector. Furthermore, as illustrated in Fig. 7(b), the photodetector also possessed eminent air stability. It was found that the

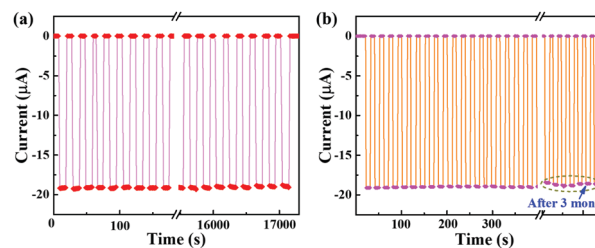


Fig. 7 (a) Time-dependent photoresponse of the CsBi<sub>3</sub>I<sub>10</sub> perovskite/Si heterojunction photodetector over 800 cycles of operation. (b) Comparison of time-dependent photoresponse of the device before and after air-storage for 3 months.

device was capable of showing reversible switching property with nearly negligible variation in photocurrent after 3 months of storage in air without any protection and encapsulation. Understandably, two factors were responsible for such a prominent long-term durability and air stability. First, as observed in our previous work, substitution of the organic component with an inorganic Cs atom can greatly increase the stability of the CsBi<sub>3</sub>I<sub>10</sub> perovskite, in comparison with the widely explored methylammonium lead halide based perovskites.<sup>25</sup> The observed good ambient stability was further confirmed by the XRD pattern of the as-synthesized CsBi<sub>3</sub>I<sub>10</sub> perovskite after 3 months of storage keeps almost unchanged (Fig. S6, ESI<sup>†</sup>). Another reason was likely due to the compact perovskite film that prevents oxidation at the surface of Si, which therefore retains the high quality of the heterojunction interface.

## Experimental section

### Materials preparation and characterization

In this work, the CsBi<sub>3</sub>I<sub>10</sub> perovskite film was prepared *via* a modified method.<sup>25</sup> In brief, 0.1 mmol CsI (99.9%, Aladdin Company) and 0.3 mmol BiI<sub>3</sub> (99.99%, Aladdin Company) were dissolved into a mixed solvent (1 ml) containing *N,N*-dimethylformamide (DMF) and dimethyl sulfoxide (DMSO) with a volume ratio of 4:1 to produce the precursor solution. The as-mixed solution was then ultrasonically treated for 30 min to facilitate dissolution of the chemicals. After that, the solution was filtered by a polytetrafluoroethylene (PTFE) filter paper and heated up to 65 °C for 15 min prior to use. The CsBi<sub>3</sub>I<sub>10</sub> perovskite film was fabricated by directly spin-coating the precursor solution onto a clean glass substrate treated by oxygen plasma for 5 min at a speed of 1500 rpm for 60 s, followed by rinsing with a solvent of chloroform (CHCl<sub>3</sub>, 1 ml). To improve the crystal quality of the film, the as-assembled sample was then dried in a vacuum at 120 °C for 30 min. The morphology of the perovskite film was characterized by a field-emission scanning electron microscope (the Sirion 200 field emission gun). The X-ray diffraction (XRD) measurement was conducted by an X-ray diffractometer (Rigaku D/Max-rB) to investigate the crystal structure of the film. The X-ray photoelectron spectroscopy (XPS) analysis was carried out using a monochromatic Al K $\alpha$  source (1486.6 eV) created by an XPS system (ESCALAB 250Xi) to study the composition of the sample.

The absorption spectrum was recorded on an UV/vis/NIR spectrophotometer (Cary 5000). An ultraviolet photoelectron spectroscope (ESCALAB 250) was employed to study the electronic structure of the perovskite.

### Device fabrication and characterization

To fabricate the heterojunction photodetector, a SiO<sub>2</sub> (300 nm)/Si (resistivity: 1–10 Ω cm<sup>-1</sup>) substrate with an open window of 0.01 cm<sup>2</sup> was firstly prepared by removing the SiO<sub>2</sub> insulating layer through a combined photolithography and wet etching process, which defines the effective area of the device. Then, the substrate was sequentially spin-coated with the above precursor solution at 1500 rpm for 60 s, rising with CHCl<sub>3</sub>, and dried in a vacuum at 120 °C for 30 min, and the heterojunction was formed within the open window area. Afterwards, a Au (50 nm) electrode was deposited on the perovskite surface near the open window area through electron-beam evaporation, and an In–Ga alloy electrode was attached to the rear side of the Si substrate, to establish electrical contacts with the perovskite and n-Si, respectively. The electrical property of the heterojunction device was probed using a semiconductor characterization system (4200-SCS, Keithley Co. Ltd). An 808 nm laser diode (Thorlab Company) was employed as the light source to study the photoresponse property. To study response speed, the laser diode was driven by a function generator (Tektronix, TDS2022B) to produce pulsed light of varied frequencies, and a digital oscilloscope (Tektronix, TDS2012B) was employed to record the electrical data. The spectral response was investigated by employing a lab-built optoelectronic system containing a light source (LE-SP-LS-XE) and a monochromator (LE-SP-M300). Prior to measurement, the light intensity of all light sources was carefully calibrated using a power meter (Thorlabs GmbH., PM 100D). All measurements were conducted under ambient conditions at room temperature.

## Conclusions

In summary, we fabricated a sensitive NIR photodetector based on a heterojunction of CsBi<sub>3</sub>I<sub>10</sub> perovskite/Si by directly depositing a layer of perovskite onto a planar Si substrate. The remarkable photovoltaic activity endowed the heterojunction with a capability of working as a self-driven photodetector, which displayed good photoresponse performance with a high  $I_{\text{light}}/I_{\text{dark}}$  ratio of  $\sim 1 \times 10^4$ , a large responsivity of 178.7 mA W<sup>-1</sup>, a decent EQE of 27.2%, a good specific detectivity of  $4.99 \times 10^{10}$  Jones, and a fast response rate of 73/36 μs under 808 nm illumination. What is more, the responsivity, EQE and specific detectivity values can be further improved to as high as 492.1 mA W<sup>-1</sup>, 75.2% and  $1.38 \times 10^{11}$  Jones at an operational bias of -1 V. Photoresponse analysis also found that the photodetector exhibited sensitivity to a broad spectral region with maximum sensitivity at  $\sim 820$  nm. In addition, the present heterojunction photodetector held outstanding durability and long-term stability under ambient conditions. Taking advantage of the good device performance and facile solution processability, it is expected

that such an inorganic perovskite/Si heterojunction photodetector will find critical applications in future low-cost and efficient NIR photodetection.

## Conflicts of interest

There are no conflicts to declare.

## Acknowledgements

This work was supported by the National Natural Science Foundation of China (NSFC no. 61575059, 21501038), and the Fundamental Research Funds for the Central Universities (2013HGCH0012, 2014HGCH0005, JZ2018HGPD0275, and JZ2018HGTA0220).

## Notes and references

- 1 A. Kojima, K. Teshima, Y. Shirai and T. Miyasaka, *J. Am. Chem. Soc.*, 2009, **131**, 6050–6051.
- 2 J. Burschka, N. Pellet, S. J. Moon, R. Humphry-Baker, P. Gao, M. K. Nazeeruddin and M. Grätzel, *Nature*, 2013, **499**, 316–319.
- 3 M. M. Lee, J. Teuscher, T. Miyasaka, T. N. Murakami and H. J. Snaith, *Science*, 2012, **338**, 643–647.
- 4 K. Domanski, E. A. Alharbi, A. Hagfeldt, M. Grätzel and W. Tress, *Nat. Energy*, 2018, **3**, 61–67.
- 5 Z. Tan, J. Li, C. Zhang, Z. Li, Q. Hu, Z. Xiao, T. Kamiya, H. Hosono, G. Niu, E. Lifshitz, Y. Cheng and J. Tang, *Adv. Funct. Mater.*, 2018, **28**, 1801131.
- 6 W. Deng, X. Xu, X. Zhang, Y. Zhang, X. Jin, L. Wang, S. T. Lee and J. Jie, *Adv. Funct. Mater.*, 2016, **26**, 4797–4802.
- 7 J. Xing, F. Yan, Y. Zhao, S. Chen, H. Yu, Q. Zhang, R. Zeng, H. V. Demir, X. Sun, A. Huan and Q. Xiong, *ACS Nano*, 2016, **10**, 6623–6630.
- 8 H. Zhu, Y. Fu, F. Meng, X. Wu, Z. Gong, Q. Ding, M. V. Gustafsson, M. T. Trinh, S. Jin and X. Y. Zhu, *Nat. Mater.*, 2015, **14**, 636–642.
- 9 Q. Zhang, S. T. Ha, X. Liu, T. C. Sum and Q. Xiong, *Nano Lett.*, 2014, **14**, 5995–6001.
- 10 Y. Lee, J. Kwon, E. Hwang, C. H. Ra, W. J. Yoo, J.-H. Ahn, J. H. Park and J. H. Cho, *Adv. Mater.*, 2015, **27**, 41–46.
- 11 H. R. Xia, J. Li, W. T. Sun and L. M. Peng, *Chem. Commun.*, 2014, **50**, 13695–13697.
- 12 L. Dou, Y. Yang, J. You, Z. Hong, W. H. Chang, G. Li and Y. Yang, *Nat. Commun.*, 2014, **5**, 5404.
- 13 H. Sun, W. Tian, F. Cao, J. Xiong and L. Li, *Adv. Mater.*, 2018, **30**, 1706986.
- 14 H. Wang and D. H. Kim, *Chem. Soc. Rev.*, 2017, **46**, 5204–5236.
- 15 M. Ahmadi, T. Wu and B. Hu, *Adv. Mater.*, 2017, **29**, 1605242.
- 16 W. Tian, H. Zhou and L. Li, *Small*, 2017, **13**, 1702107.
- 17 J. Zhou and J. Huang, *Adv. Sci.*, 2018, **5**, 1700256.
- 18 C. Xie, P. You, Z. Liu, L. Li and F. Yan, *Light: Sci. Appl.*, 2017, **6**, e17023.

- 19 C. Xie and F. Yan, *ACS Appl. Mater. Interfaces*, 2017, **9**, 1569–1576.
- 20 Z. Xiao, Y. Yuan, Y. Shao, Q. Wang, Q. Dong, C. Bi, P. Sharma, A. Gruverman and J. Huang, *Nat. Mater.*, 2015, **14**, 193–198.
- 21 Y. Wang, Z. Xia, S. Du, F. Yuan, Z. Li, Z. Li, Q. Dai, H. Wang, S. Luo, S. Zhang and H. Zhou, *Nanotechnology*, 2016, **27**, 175201.
- 22 Z. X. Zhang, L. H. Zeng, X. W. Tong, Y. Gao, C. Xie, Y. H. Tsang, L. B. Luo and Y. C. Wu, *J. Phys. Chem. Lett.*, 2018, **9**, 1185–1194.
- 23 D. Parobek, B. J. Roman, Y. Dong, H. Jin, E. Lee, M. Sheldon and D. H. Son, *Nano Lett.*, 2016, **16**, 7376–7380.
- 24 A. Waleed, M. M. Tavakoli, L. Gu, Z. Wang, D. Zhang, A. Manikandan, Q. Zhang, R. Zhang, Y. L. Chueh and Z. Fan, *Nano Lett.*, 2017, **17**, 523–530.
- 25 X. W. Tong, W. Y. Kong, Y. Y. Wang, J. M. Zhu, L. B. Luo and Z. H. Wang, *ACS Appl. Mater. Interfaces*, 2017, **9**, 18977–18985.
- 26 C. Xie, Y. Wang, Z. X. Zhang, D. Wang and L. B. Luo, *Nano Today*, 2018, **19**, 41–83.
- 27 Y. Fang and J. Huang, *Adv. Mater.*, 2015, **27**, 2804–2810.
- 28 Q. Lin, A. Armin, D. M. Lyons, P. L. Burn and P. Meredith, *Adv. Mater.*, 2015, **27**, 2060–2064.
- 29 L. Shen, Y. Fang, D. Wang, Y. Bai, Y. Deng, M. Wang, Y. Lu and J. Huang, *Adv. Mater.*, 2016, **28**, 10794–10800.
- 30 M. Buscema, J. O. Island, D. J. Groenendijk, S. I. Blanter, G. A. Steele, H. S. J. van der Zant and A. Castellanos-Gomez, *Chem. Soc. Rev.*, 2015, **44**, 3691–3718.
- 31 C. Xie, C. Mak, X. Tao and F. Yan, *Adv. Funct. Mater.*, 2017, **27**, 1603886.
- 32 M. B. Johansson, H. Zhu and E. M. J. Johansson, *J. Phys. Chem. Lett.*, 2016, **7**, 3467–3471.
- 33 C. Xie, B. Nie, L. Zeng, F. X. Liang, M. Z. Wang, L. Luo, M. Feng, Y. Yu, C. Y. Wu, Y. Wu and S. H. Yu, *ACS Nano*, 2014, **8**, 4015–4022.
- 34 S. M. Sze and K. K. Ng, *Physics of Semiconductor Devices*, 2007.
- 35 Y. Zhao and K. Zhu, *Chem. Soc. Rev.*, 2016, **45**, 655–689.
- 36 Z. Liang, P. Zeng, P. Liu, C. Zhao, W. Xie and W. Mai, *ACS Appl. Mater. Interfaces*, 2016, **8**, 19158–19167.
- 37 L. H. Zeng, M. Z. Wang, H. Hu, B. Nie, Y. Q. Yu, C. Y. Wu, L. Wang, J. G. Hu, C. Xie, F. X. Liang and L. B. Luo, *ACS Appl. Mater. Interfaces*, 2013, **5**, 9362–9366.
- 38 X. Li, M. Zhu, M. Du, Z. Lv, L. Zhang, Y. Li, Y. Yang, T. Yang, X. Li, K. Wang, H. Zhu and Y. Fang, *Small*, 2016, **12**, 595–601.
- 39 L. Wang, J. Jie, Z. Shao, Q. Zhang, X. Zhang, Y. Wang, Z. Sun and S. T. Lee, *Adv. Funct. Mater.*, 2015, **25**, 2910–2919.
- 40 J. Liu, *Photonic Devices*, Cambridge University Press, Cambridge, 2005, vol. 1.
- 41 L. B. Luo, J. J. Chen, M. Z. Wang, H. Hu, C. Y. Wu, Q. Li, L. Wang, J. A. Huang and F. X. Liang, *Adv. Funct. Mater.*, 2014, **24**, 2794–2800.
- 42 Z. Wang, R. Yu, C. Pan, Z. Li, J. Yang, F. Yi and Z. L. Wang, *Nat. Commun.*, 2015, **6**, 8401.
- 43 H. Zhou, Z. Song, P. Tao, H. Lei, P. Gui, J. Mei, H. Wang and G. Fang, *RSC Adv.*, 2016, **6**, 6205–6208.
- 44 N. Alwadai, M. A. Haque, S. Mitra, T. Flemban, Y. Pak, T. Wu and I. Roqan, *ACS Appl. Mater. Interfaces*, 2017, **9**, 37832–37838.
- 45 Q. Hong, Y. Cao, J. Xu, H. Lu, J. He and J. L. Sun, *ACS Appl. Mater. Interfaces*, 2014, **6**, 20887–20894.
- 46 G. Li, L. Liu, G. Wu, W. Chen, S. Qin, Y. Wang and T. Zhang, *Small*, 2016, **12**, 5019–5026.